Supporting Information

Computational screening of Single and Di-atom catalysts for electrochemical CO_2 reduction

Naiwrit Karmodak*, Sudarshan Vijay, Georg Kastlunger, Karen Chan*

CatTheory, Physics Department, Denmark Technical University, Kongens Lyngby, Denmark.

Email: naikar@dtu.dk; kchan@fysik.dtu.dk

Section S-I:

Computational Details

The DFT calculations are performed using the Vienna Ab-Initio Simulation package (VASP).[1] We have used projector augmented wave potentials to describe the core electrons,[2] whereas the valence electrons are defined using the plane-wave basis function with the kinetic energy cutoff of 500 eV. A Gaussian smearing is used with a width of 0.1 eV for the relaxations and binding energy calculations of the reaction intermediates. The single and diatom (SACs and DACs respectively) doped structures are relaxed with the spin polarized RPBE functional.[3] Benchmark calculations in ref.[4] show that CO_2R intermediates show over binding to the catalytic sites. Therefore, the binding energies of the reaction intermediates on single and diatom catalysts are corrected with single-point energy calculations at hybrid HSE06 functional using the relaxed geometries obtained with RPBE functional.[5,6]

The calculations with the (211) transition metal surfaces are done with the 3x3x3 slab with the bottom two layers fixed. The SACs are modelled using a 3x3 graphene layer,[7] whereas for DACs we have used a 5x3 graphene layer. The structures are prepared using the Atomic Simulation Environment (ASE) package.[8] The lattice relaxations of the bulk metal surfaces and graphene are done with a 12x12x1 Monkhorst-Pack k-point mesh.[9] On the other hand, the HSE

calculations on the supercells of the graphene layers with single and di-atom metal dopants are performed with 3x4 and 2x2 Monkhorst-Pack k-point meshes. The geometries are optimized until the forces are lower than 0.025 eV $Å^{-1}$. The reaction free energies at 298.15 K are obtained from the DFT calculated energies using the vibrations from the VASP simulations. The ASE Thermochemistry class is used to determine the Helmholtz and Gibbs free energies from the harmonic thermochemistry and ideal gas thermochemistry respectively for adsorbed and gaseous species.[8]

The solvent and electrolyte effects are considered using a continuum solvation model implemented in VASPsol package.[10] A continuum implicit charge distribution is defined in the vacuum region of the simulation cell with the charge density of opposite sign corresponding to the excess surface charge of the 2D material slab. A Debye screening of 3 Å is used, which corresponds to the bulk ion concentration of 1 M. The non-electrostatic parameter TAU is taken as zero to avoid the numerical instabilities.[11]

The reaction energetics as a function of the applied potential with the proton-electron pair are determined using the computational hydrogen electrode (CHE) method.[12] The chemical potential of proton is related to H_2 at 0 V with respect to the reversible hydrogen electrode as defined by the following equation:

$$\mu_{H^+} + \mu_{e^-} = \frac{1}{2}\mu_{H_2} \text{ (eq. S1)}$$

The potential dependence on the adsorption free energy calculations is defined using the surface-adsorbate dipole-field interactions following a similar method as described in ref [4,13]. A linear dependence of the binding energies is considered with respect to the surface charge values (σ) as given by the following equation:

$$\Delta G = \Delta G_o + \mu|\overrightarrow{\varepsilon}| \text{ (eq. S2)}$$

Here the coefficients ΔG_o and μ correspond to energy with zero charge and dipole moment respectively. $\overrightarrow{|\varepsilon|}$ is the interfacial electric field. The surface charge density (σ) and $\overrightarrow{|\varepsilon|}$ can be related by Gauss law. Assuming a linear fit of the adsorption energy and surface charge density (σ), we have obtained the intercept (ΔG_o) and slope (μ) values. The linear dependence of energy with the surface charge σ considered here is valid for small variation of the electronic charges of the unit cell. At large variation of the surface charges, second order terms are important. In our calculations, we have seen that adsorption energies show a linear dependence with respect to the applied small surface charges.

In recent studies on single atom catalysts in ref.[4,14], the linear dependence for the interactions between the polar adsorbates and interfacial electric fields are found to effectively define the pH dependencies on the experimental Tafel slopes for CO_2R. Further validation of this approach and comparison with the grand canonical ensemble DFT methods are shown in ref.[4,11,14,15]

We have related the surface charge (σ) to the potential (ϕ) using the following eq:

$$\phi = \frac{1}{C}\sigma + \phi_{pzc} \text{ (eq. S3)}$$

A capacitance (C) value of 21 $\mu F/cm^2$ and experimental potential of zero charge (ϕ_{pzc}) value of 0.07 V is used for pristine graphene.[16,17] Vacancy sites and metal dopants are expected to change the PZC value if present in high concentration. We approximated all our catalysts to have identical PZC values in this study. Our assumptions are based upon the recent experimental studies on the catalytic activity of SACs and possible doping concentrations of the metal atoms on the vacancy sites of graphene for single and diatom catalysts. The recent studies have found that for SACs, the doping concentrations are between 2 to 3% by weight.[18] It is found to be similar for diatom catalysts.[19,20] We expect that with lower doping concentration of the metal atoms, the PZC value of the pristine graphene would be negligibly affected.

Microkinetic Modelling of reaction pathways:

The unified activity volcano plots and the coverage plots shown in the main text and supporting information is calculated based upon the following kinetic model:

$$\text{rate} = k_+ \Pi\theta_{react}\Pi p_{react} - k_- \Pi\theta_{prod}\Pi p_{prod} \text{ (eq. S4)}$$

Here, + and – indicates the forward and backward reaction pathways. The rate constant values k_+ and k_- are defined by $k_+ = Aexp(-\frac{G_{a+}}{k_B T})$ and $k_- = Aexp(-\frac{G_{a-}}{k_B T})$ respectively. G_{a+} *and* G_{a-} are the free energy barriers of the reaction pathways and A is the prefactor. In the absence of reaction barriers, the reaction free energy values at an applied potential are used to estimate the reaction barriers as given by $\Delta G = \Delta G^o + neU + \Delta G_{field}$. Here, ΔG^o is the reaction free energy at 0 applied potential in V vs SHE, n is the number of proton-electron transferred and the dipole-filed interactions are given by ΔG_{field} ($= a_1\sigma$, *as shown in eq. S2*). We have used the prefactor value of 5.78 x 10^{12}, which is equivalent to $k_B T/h$. Here, k_B is the Boltzmann constant, h is the Planck constant and T is room temp (300 K). θ_i and p_i refer to the coverage of adsorbed intermediates and partial pressure of gaseous species respectively.

Microkinetic modelling of the reaction pathways is performed using the CatMAP (https://catmap.readthedocs.io/en/latest/),[21] which uses the Newton-root finding algorithm to calculate the rates and coverages. A decimal precision of 100 in addition to a convergence tolerance value of 10^{-25} are used. The rate equations are solved numerically under steady state approximation, with the constraint from site conservation as given below:

$$\frac{\partial \theta_i}{\partial t} = 0 \text{ , for steps in steady state (eq. S5)}$$

$$\theta_* + \theta_{*CO_2} + \theta_{*COOH} + \theta_{*CO} = 1 \text{ (eq. S6)}$$

The TOF values used to define the activity of the catalyst in the volcano plots correspond to the rate of the reactions computed per active site of the catalysts.

In the previous studies with the single atom catalysts,[4, 14] the kinetic barriers for CO_2 to CO reduction are found to have minimal effect on the kinetic modeling or are appropriately estimated by the reaction free energies. Under relevant applied potential, the $*CO_2$ adsorption is found to have the highest free energy. The subsequent steps from *COOH to *CO show high exergonicity with no additional barrier under reducing potential. Since the adsorption energy of $*CO_2$ shows a similar potential dependence as the final adsorbed state, it is found that adsorption energy gives a good estimation of the adsorption barrier (differences between reaction energies and adsorption barrier is most of 0.2 eV). The diatom catalysts show a similar dipole field interactions for the reaction intermediates as the single atom catalysts. Therefore, we have used a similar approach to define the activity of the catalysts. The reaction energies are used as the inputs to develop the micro-kinetic model and the unified activity volcano plot.

Section S-II: Formation energy calculations of single and double atom catalysts:

The formation energies of the SACs and DACs are calculated using the eq. S7 as shown below.

$$\Delta E_{form} = (E_{M1/M2-NC} - E_{M1/M2(bulk)} - E_{NC})/n \text{ (eq. S7)}$$

Here, $E_{M1/M2-NC}$ denotes the energy of the SACs and DACs. The reference energies for metal dopants denoted as $E_{M1/M2}$ are obtained from the DFT calculated energies of the bulk metal. n is the number of dopant site.

The most stable geometries of SACs and DACs are obtained by geometry relaxations at RPBE functional. The formation energies are calculated using HSE06 functional using the relaxed geometries obtained with RPBE functional. For SACs, we have considered the single and double carbon atom vacancy sites as shown in Figure S1. The stable doping sites for DACs are determined by comparing the formation energies of diatom dopants on varying carbon atom vacancies varying from two to six carbon atoms as shown in Figure 1 of the main text. The Figure S2 and S3 shows the formation energies in eV per dopant site. The SACs show the highest stability with double carbon atom vacancy with 4 N atom (DV4N) coordination. On the other hand, for DACs, the highest stability is obtained for the quad-atom vacancy (QV) sites.

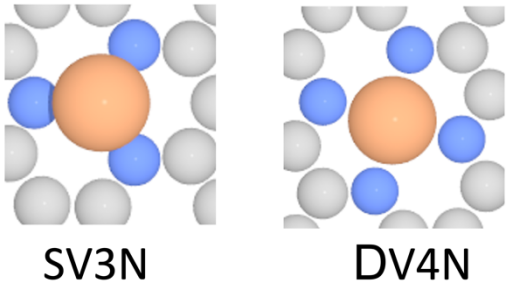

Figure S1: The single and double carbon atom vacancy dopant sites for single metal atoms sites on graphene with various numbers of surrounding N-atom coordination. The vacancy sites are denoted by two letter symbols as SV and DV corresponding to single and double carbon atom vacancies respectively.

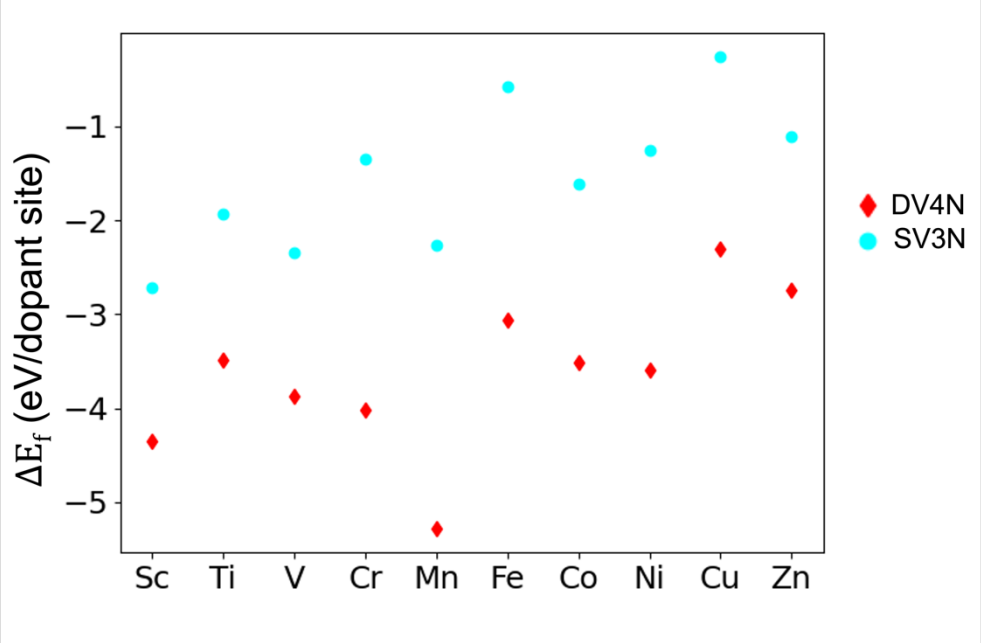

Figure S2: The formation energies (in eV/ dopant site) of SACs with single (SV) and double (DV) carbon atom vacancy sites. The SV site is denoted in solid circle, whereas the diamond marker denote the DV site. The color codes for the different N-atom coordination are given in left panel of the Figure.

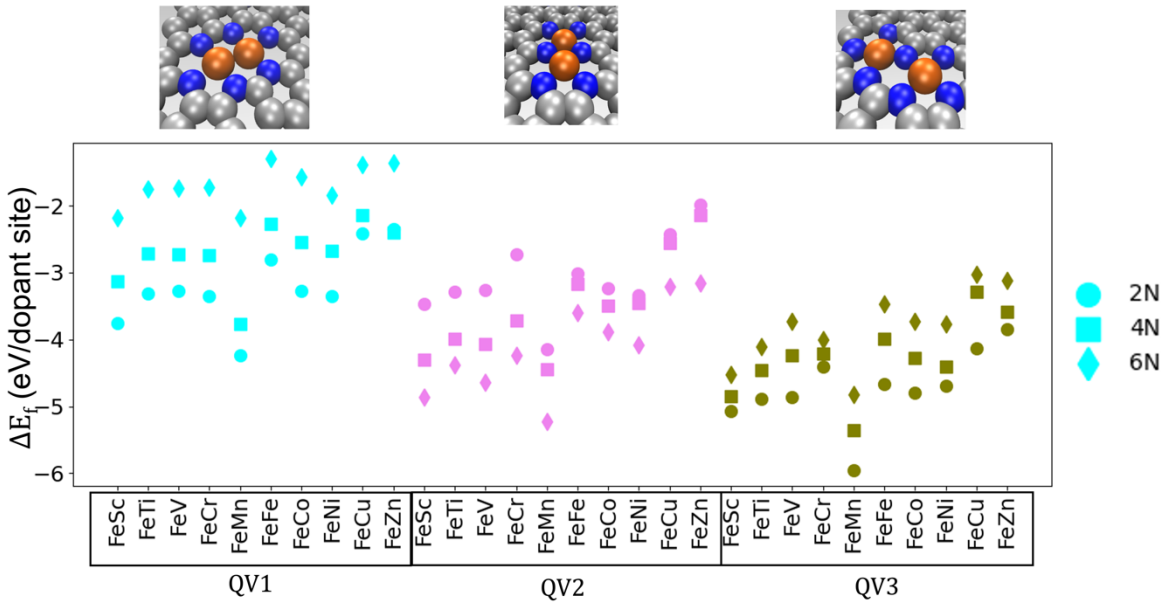

Figure S3: (a) The formation energies (in eV/ per dopant site) of FeM DACs with quadatom (QV) dopant sites for varying surrounding N atom coordination. The top panel shows the structural configuration of the diatom dopant sites for QV1, QV2 and QV3 doping sites.

Figure S3 shows that the stability of most stable QV sites with varying number of N atom coordination. Different structural polymorphs are considered by varying the N atom positions for QV(4N) and QV(2N) sites. The most stable structures are determined by the geometry

relaxation at RPBE followed by an energy correction at HSE06 functional. The formation energies are calculated following the eq. 4 (above).

We have found that the stability reduces with decrease in the number of N atom coordination for QV2 site, whereas for QV1 and QV3 sites, a reverse trend is observed. The stability increases with the decrease in surrounding N atom coordination. The stability trend shown in Figure S3 would likely influence the coverage of these doping sites on graphene. However, we believe that all these sites could be formed depending upon the synthesis conditions.

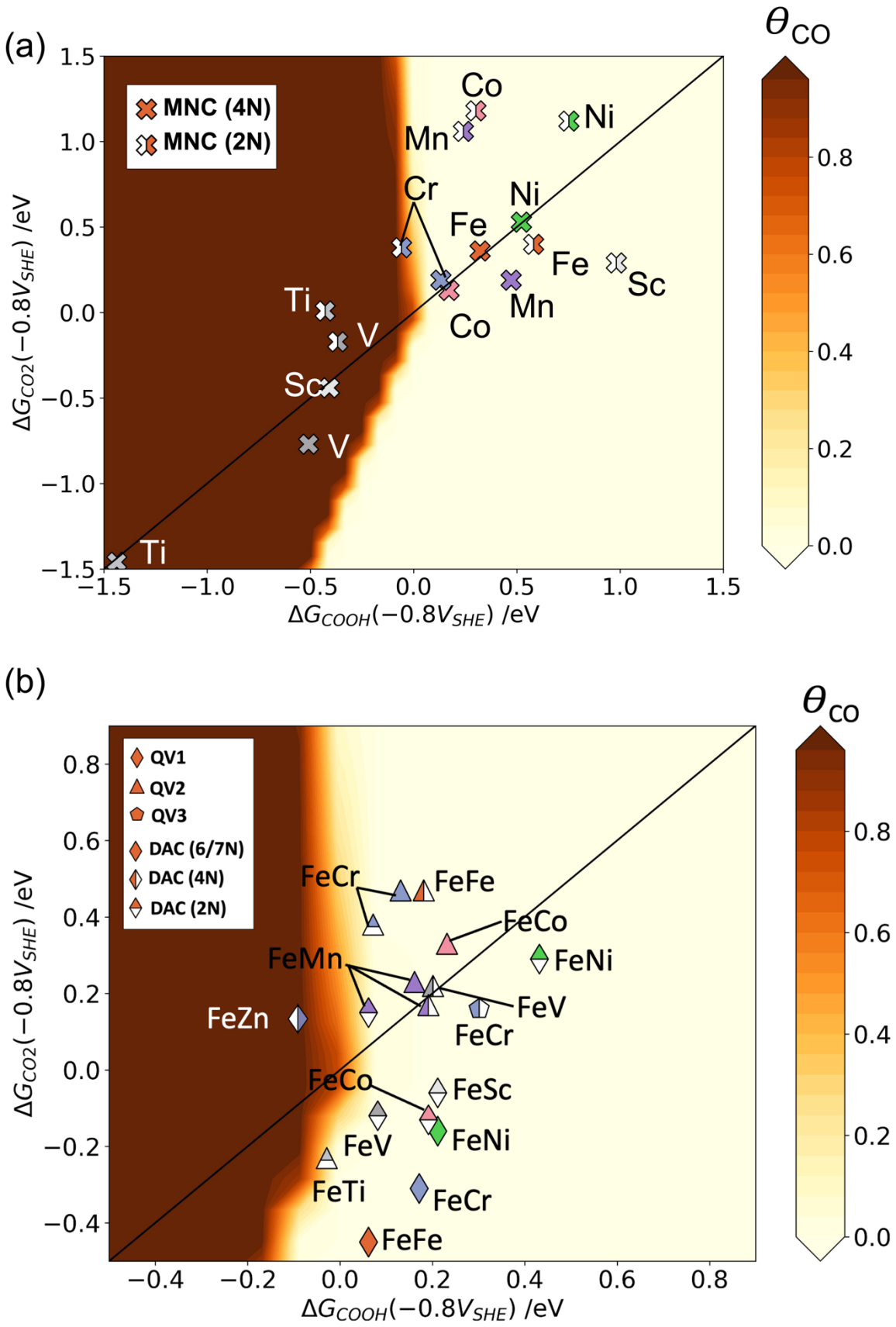
(a)
MNC (4N)
MNC (2N)
Co
Ni
Mn
Cr
Ni
Fe
Fe
Sc
Mn
Co
Ti
V
Sc
V
Ti
$\Delta G_{CO2}(-0.8V_{SHE})$ /eV
$\Delta G_{COOH}(-0.8V_{SHE})$ /eV
θ_{CO}
(b)
QV1
QV2
QV3
DAC (6/7N)
DAC (4N)
DAC (2N)
FeCr
FeFe
FeCo
FeNi
FeMn
FeV
FeZn
FeCr
FeCo
FeSc
FeNi
FeV
FeTi
FeCr
FeFe
$\Delta G_{CO2}(-0.8V_{SHE})$ /eV
$\Delta G_{COOH}(-0.8V_{SHE})$ /eV
θ_{CO}

Figure S4: CO coverage map for the SACs (a) and DACs (b) obtained using a simple mean field microkinetic model, simulated based upon the binding free energy values of CO_2^* and $COOH^*$ intermediates at -0.8 V vs SHE and pH of 6.8. The SACs and DACs with TOF comparable to or greater than Au (211) surfaces as identified in the activity volcano plot shown in Figure 3 of the main text and CO coverage less than 0.4 are shown here.

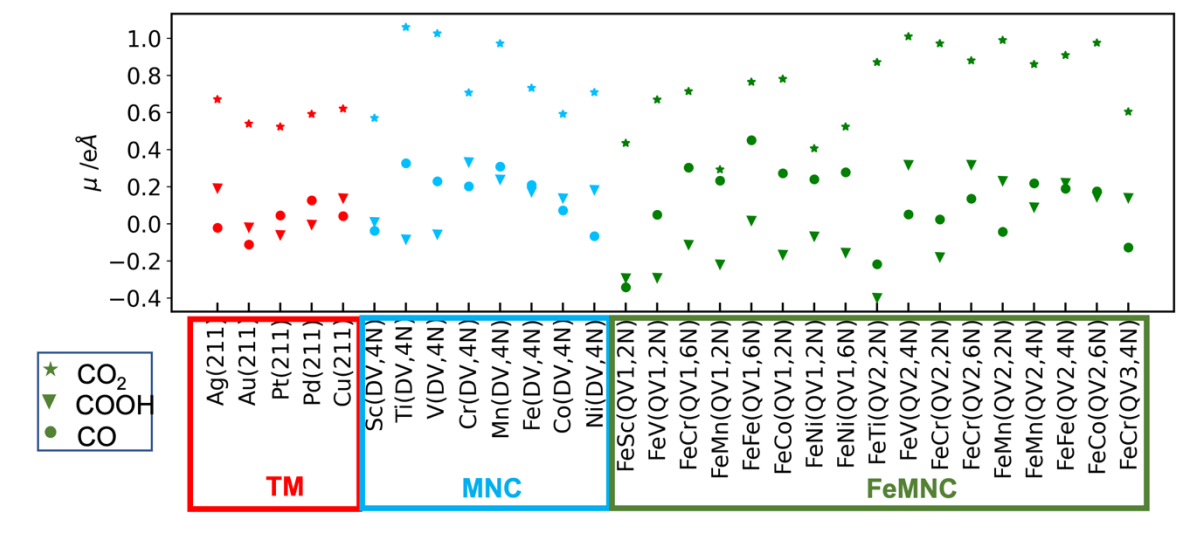

Figure S5: The adsorbate dipole moment of the CO_2R intermediates on TM (211) surface, SACs, and DACs. For SACs and DACs, the metal dopants with TOF comparable to or greater than Au (211) surface are shown here. The dipole moment values are calculated based upon the change in the electron density values as captured using the eq: $\mu = \int \rho \, dz$, where ρ is the charge density and z is the axis of integration. The adsorbate dipole moments for CO_2^* is found to be greater than both $COOH^*$ and CO^* intermediates.

Section S-III: Potential dependence of activity rate map of SACs and DACs.

In this section, the potential dependence of the activity rate map for the SACs and DACs are shown. The activity is calculated based upon the binding free energies of CO_2^* and $COOH^*$ intermediates at potential -0.6, -0.8, -1.0 and -1.2 V vs SHE and buffer pH of 6.8. The SACs and DACs are denoted using the different markers as shown in Figure insets. The black dotted line shows the scaling line of the five TM (211) surfaces. The black solid line corresponds to the parity line. Deviation from this line would lead either of the two reaction steps, $CO_2(g) + * \rightleftharpoons CO_2^*$ or $COOH^* + H^+ + e^- \rightleftharpoons CO^* + H_2O$ to be the rate limiting step as discussed in the main text. The single and dimer metal dopants with TOF similar or greater than Au (211) surface are shown in solid markers, whereas the less active materials are shown in faded markers. The black dotted region shows the rate map of Au (211) surfaces. The markers with solid black outlines corresponds to the materials with formation energy comparable to FeNC SAC.

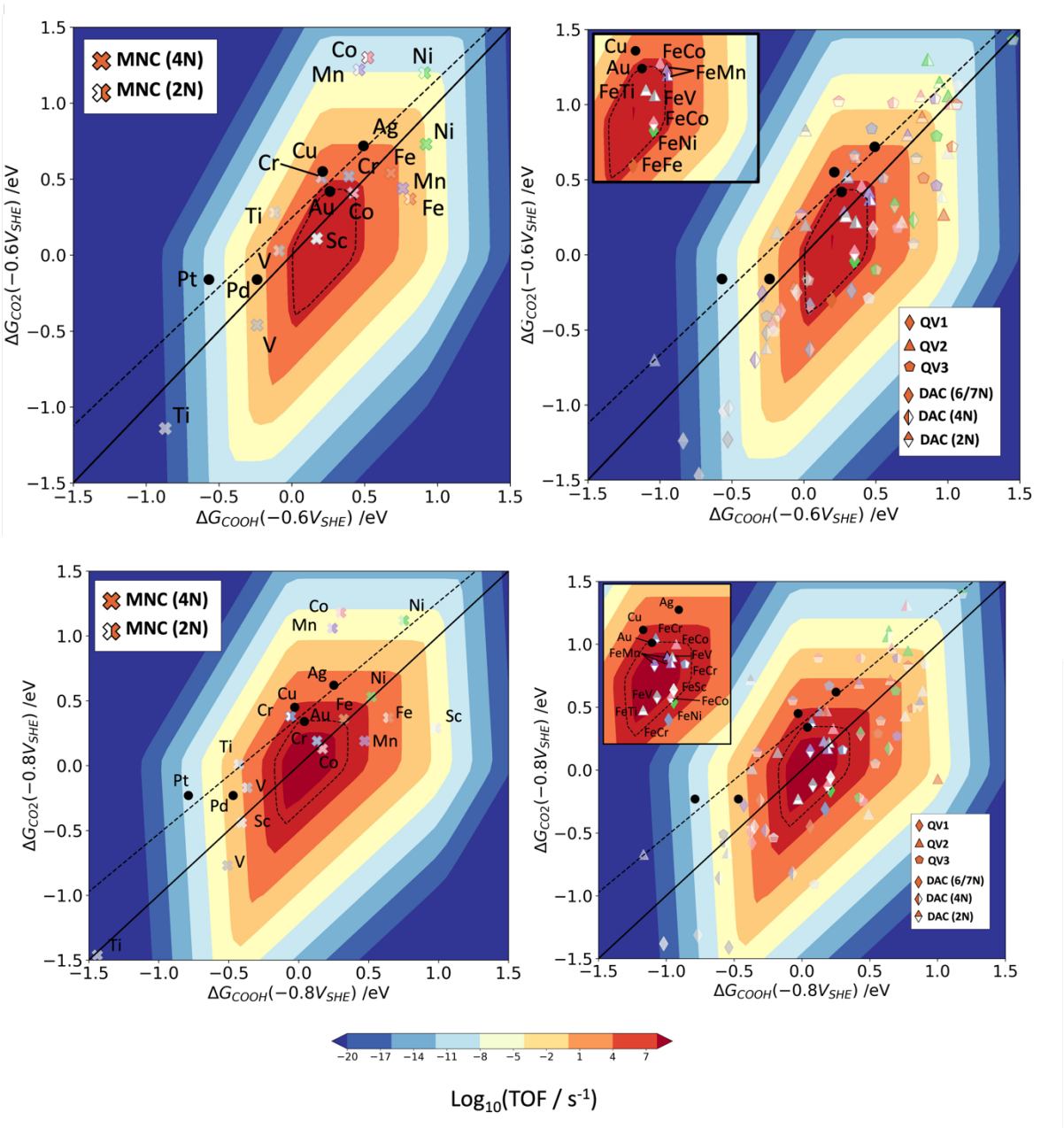

Figure S6: Activity rate map for SACs and DACs at -0.6 and -0.8 V vs SHE and pH of 6.8. The left panel shows the activity for the SACs and right panel shows activity of the DACs.

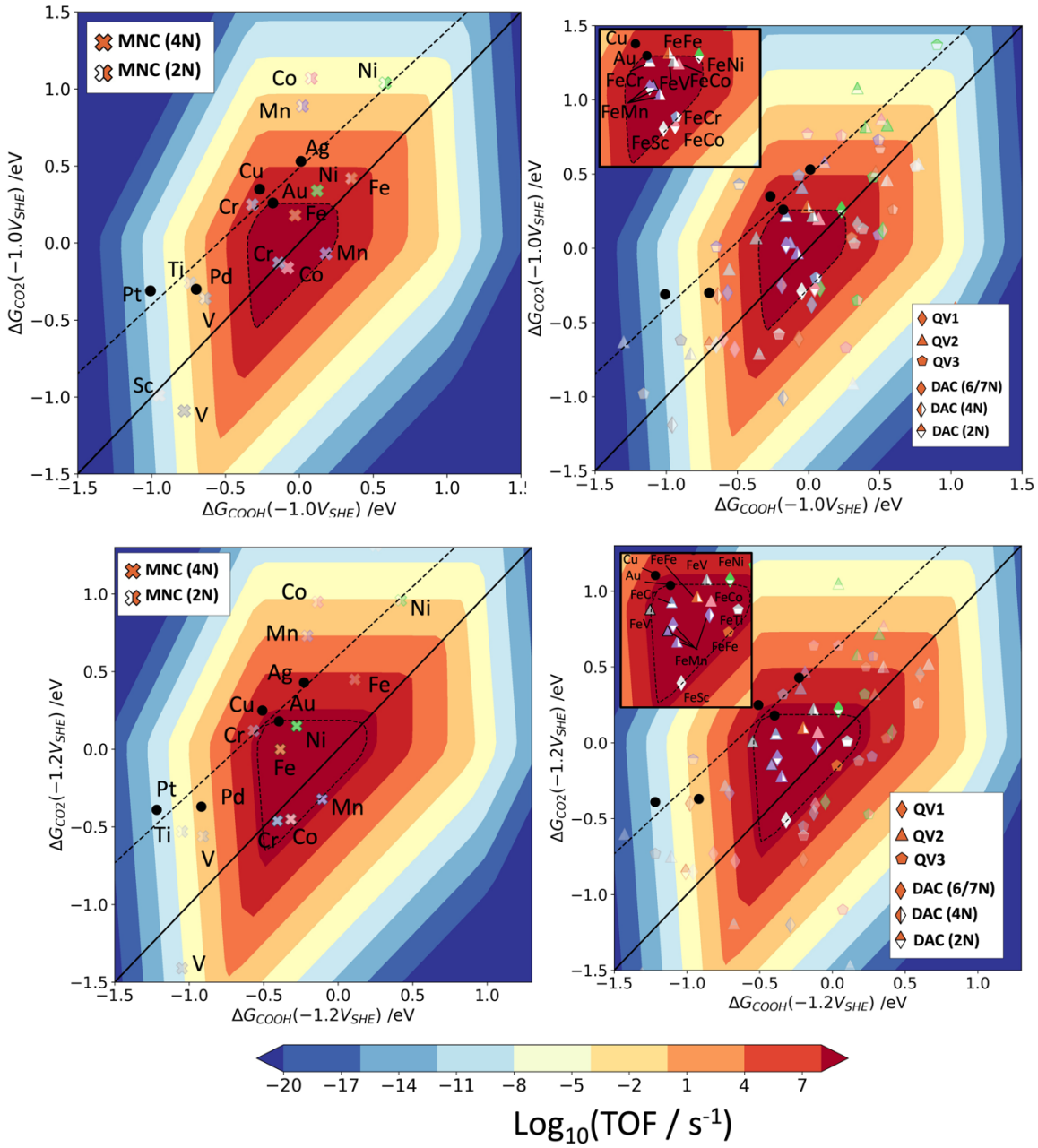

Figure S7: Activity rate map for SACs and DACs at -1.0 and -1.2 V vs SHE and pH of 6.8. The left panel shows the activity for the SACs and right panel shows activity of the DACs.

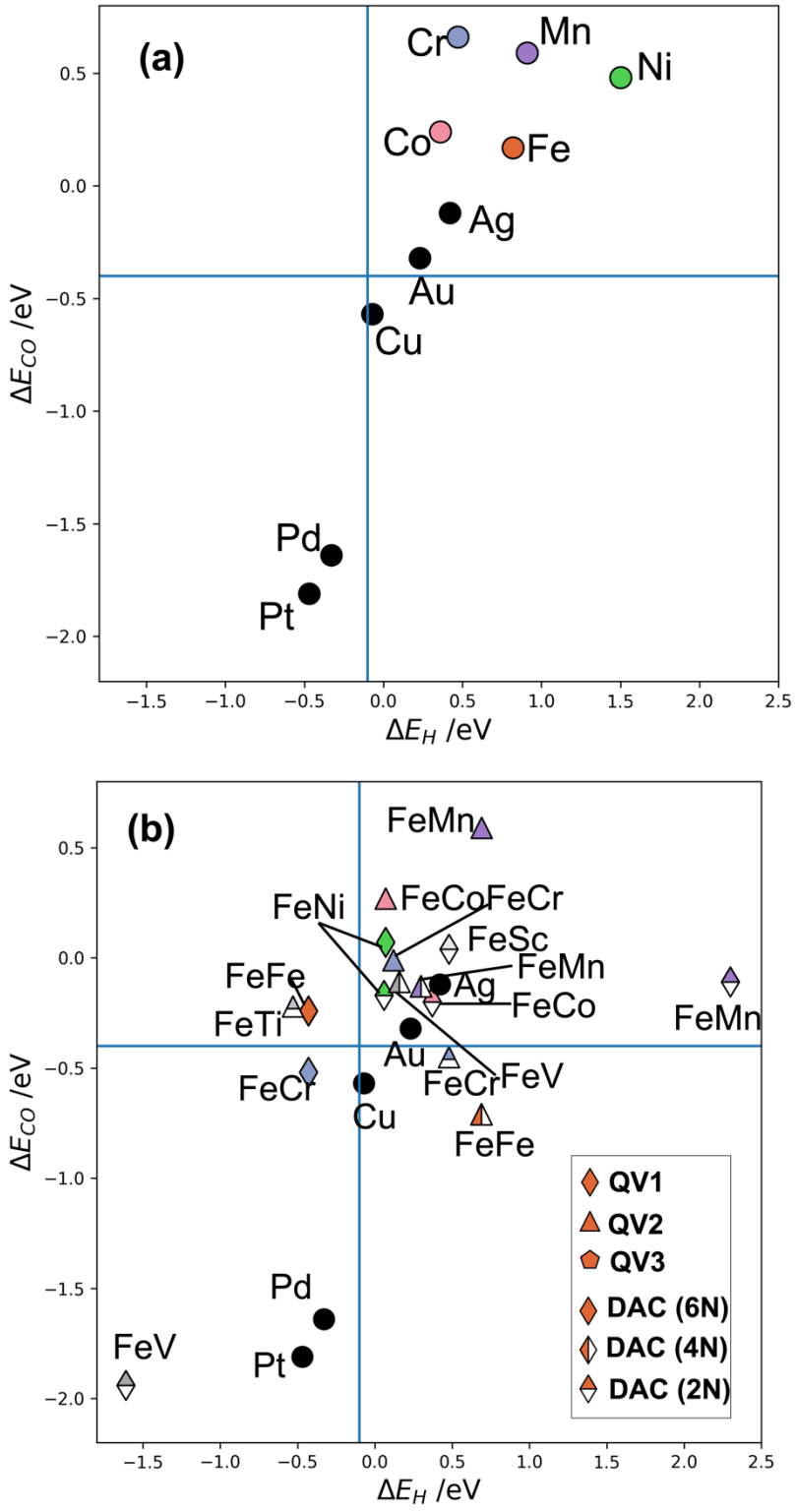

Figure S8: The classification of the best performing SACs (a) and DACs (b) shown in the activity volcano plots in Figure 3(a,b) in main text for hydrogen evolution reaction and CO_2 reduction reaction based upon the binding energies of H* and CO on (111) surfaces of transition and coinage metals following the criterion of Bagger et. al.[22] All the SACs with

higher activity are found to be less selective for HER. However, for the DACs, we find that four candidates show greater binding affinity for H^* and therefore would have higher selectivity for HER.

S-IV Formation free energies of the most active diatom catalysts.

The formation free energies of the most active candidates with TOF comparable to or greater than Au (211) surface obtained from the activity volcano plot is shown here. The formation free energy values are calculated by adding the vibrational frequency contributions (ΔE_{corr}) to the formation energy (ΔE_{form}) values calculated using equation 1 shown in the main text. The doping sites and the number of coordinating N atoms are given within the brackets for each DACs. The formation free energies are reported here at 1000K, since most of the recent experiments report the formation of the DACs around this temp.[19,20]

Table S1: Formation free energies (ΔG_{form}) of the most active diatom catalysts identified in this study.

Dimer	$\Delta G_{form} = \Delta E_{form} + \Delta E_{corr}$ (eV/dopant site)
FeSc (QV1, 2N)	-3.82
FeMn (QV1, 2N)	-3.85
FeCo (QV1, 2N)	-3.53
FeNi (QV1, 6N)	-2.07
FeCr (QV2, 2N)	-3.30
FeMn (QV2, 4N)	-3.71
FeV (QV2, 4N)	-3.85
FeCo (QV2, 6N)	-3.56
FeMn (QV2, 6N)	-4.30
FeCr (QV3, 4N)	-3.92

Section S-V: Comparison of $*CO_2$ and *OCO binding motifs on DACs.

To understand the selectivity of formate pathway with respect to the CO formation pathway, we have compared the binding energies of the different CO_2 motifs on the most active diatom catalysts identified in the activity volcano plot in Figure 3 (main text) at -0.8 V vs SHE and pH of 6.8. The $*CO_2$ binding motif (CO_2 binding through C atom) is expected to form the initial precursor for CO formation pathway, whereas *OCO motif (binding through the O atoms) would form the initial precursor for the formate pathway. The six diatom catalysts obtained with higher CO_2 to CO activity do not show a preferable binding motif for *OCO. The other five DACs for which we have obtained a minimum energy structure for *OCO motif, the corresponding binding free energies for the two different motifs are shown at -0.8 V vs SHE is given in Table S2. Due to higher endothermicity of *OCO binding motif vs $*CO_2$ motif at -0.8 V vs SHE, the CO formation pathway would be more favorable than the formate pathway.

Table S2: Comparison of *CO_2 vs *OCO binding motif of CO2 on the most active DACs

Dimers	ΔG_{*CO_2}(eV)	ΔG_{*OCO}(eV)
FeSc (QV1, 2N)	-0.06	0.99
FeCr (QV1, 2N)	0.52	1.05
FeMn(QV1,2N)	0.15	1.64
FeV (QV2, 4N)	0.22	0.82
FeMn (QV2, 4N)	0.17	1.28

Section S-VI: Comparison RPBE binding energies with HSE06 functional

A comparison of the binding energies of the intermediates obtained with RPBE functional and those obtained with HSE06 with and without complete relaxation of the geometries for FeNi diatom catalysts is shown here. We have found that RPBE functional shows large differences in the binding energies of the intermediates with respect to HSE06 functional. While single point energy corrections at HSE06 functional on RPBE optimized geometries also found to show slight deviation from the binding energies obtained from the relaxed structure, however the energy difference is found to be very less (maximum deviation is 0.1 eV for *COOH and *CO). The magnetic moment values obtained from relaxation calculation and single point energy calculation with HSE06 and from RPBE functionals are very similar.

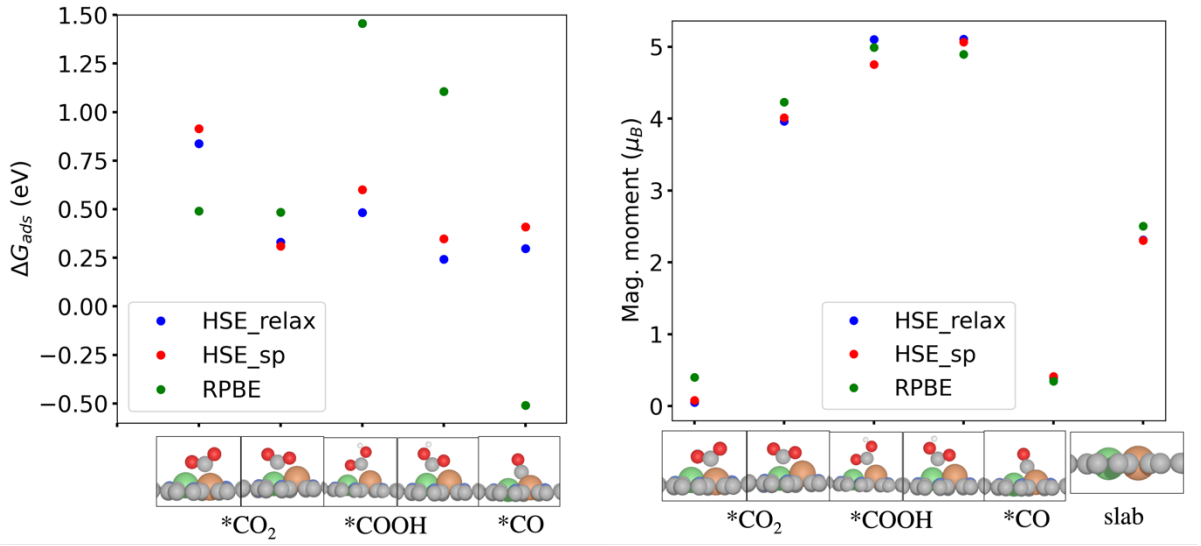

Figure S9: Comparison of RPBE energy and magnetic moment values with HSE06 calculation for CO_2R intermediates on FeNi DAC catalyst.

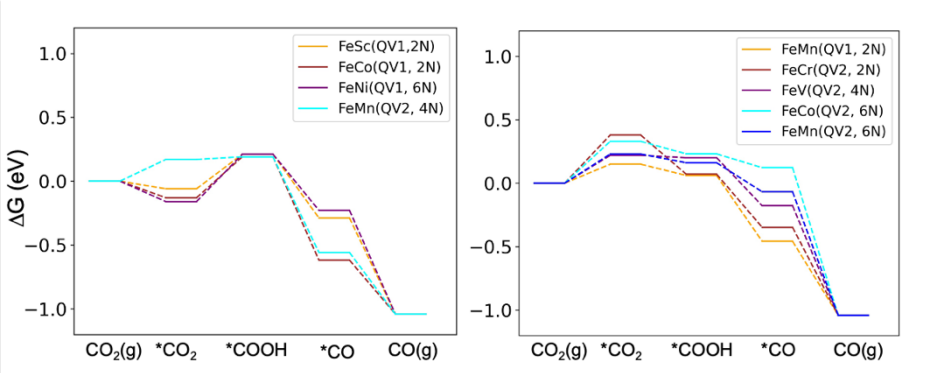

Figure S10: The free energy diagram (FED) for CO_2 to CO reduction pathway at -0.8 V vs SHE and pH of 6.8 for the most active candidates obtained from the activity volcano plot (Figure 3) and lower CO coverage. The first figure shows the FED for the catalysts for which $CO_2^* \rightarrow COOH^*$ has been found to be the rate limiting step. The second figure show the FED plot for the candidates with $CO_2(g) \rightarrow CO_2^*$ as the rate limiting step.

Supplementary References

(1) Kresse, G.; Furthmüller, J. Efficient Iterative Schemes for Ab Initio Total-Energy Calculations Using a Plane-Wave Basis Set. *Phys. Rev. B* **1996**, *54* (16), 11169–11186. https://doi.org/10.1103/PhysRevB.54.11169.

(2) Kresse, G.; Joubert, D. From Ultrasoft Pseudopotentials to the Projector Augmented-Wave Method. *Phys. Rev. B* **1999**, *59* (3), 1758–1775. https://doi.org/10.1103/PhysRevB.59.1758.

(3) Hammer, B.; Hansen, L. B.; Nørskov, J. K. Improved Adsorption Energetics within Density-Functional Theory Using Revised Perdew-Burke-Ernzerhof Functionals. *Phys. Rev. B* **1999**, *59* (11), 7413–7421. https://doi.org/10.1103/PhysRevB.59.7413.

(4) Vijay, S.; Gauthier, J. A.; Heenen, H. H.; Bukas, V. J.; Kristoffersen, H. H.; Chan, K. Dipole-Field Interactions Determine the CO2 Reduction Activity of 2D Fe–N–C Single-Atom Catalysts. *ACS Catal.* **2020**, *10* (14), 7826–7835.

(5) Heyd, J.; Scuseria, G. E.; Ernzerhof, M. Hybrid Functionals Based on a Screened Coulomb Potential. *J. Chem. Phys.* **2003**, *118* (18), 8207–8215.

(6) Ge, H. J. S.; Ernzerhof, M. Erratum:"Hybrid Functionals Based on a Screened Coulomb Potential"[J. Chem. Phys. 118, 8207 (2003)]. *J Chem Phys* **2006**, *124*, 219906.

(7) Tripkovic, V.; Vanin, M.; Karamad, M.; Björketun, M. E.; Jacobsen, K. W.; Thygesen, K. S.; Rossmeisl, J. Electrochemical CO2 and CO Reduction on Metal-Functionalized Porphyrin-like Graphene. *J. Phys. Chem. C* **2013**, *117* (18), 9187–9195. https://doi.org/10.1021/jp306172k.

(8) Larsen, A. H.; Mortensen, J. J.; Blomqvist, J.; Castelli, I. E.; Christensen, R.; Du\lak, M.; Friis, J.; Groves, M. N.; Hammer, B.; Hargus, C.; Hermes, E. D.; Jennings, P. C.; Jensen, P. B.; Kermode, J.; Kitchin, J. R.; Kolsbjerg, E. L.; Kubal, J.; Kaasbjerg, K.; Lysgaard, S.; Maronsson, J. B.; Maxson, T.; Olsen, T.; Pastewka, L.; Peterson, A.; Rostgaard, C.; Schiøtz, J.; Schütt, O.; Strange, M.; Thygesen, K. S.; Vegge, T.; Vilhelmsen, L.; Walter, M.; Zeng, Z.; Jacobsen, K. W. The Atomic Simulation Environment—a Python Library for Working with Atoms. *Journal of Physics: Condensed Matter* **2017**, *29* (27), 273002. https://doi.org/10.1088/1361-648x/aa680e.

(9) Monkhorst, H. J.; Pack, J. D. Special Points for Brillouin-Zone Integrations. *Phys. Rev. B* **1976**, *13* (12), 5188–5192. https://doi.org/10.1103/PhysRevB.13.5188.

(10) Mathew, K.; Kolluru, V. S. C.; Mula, S.; Steinmann, S. N.; Hennig, R. G. Implicit Self-Consistent Electrolyte Model in Plane-Wave Density-Functional Theory. *The Journal of Chemical Physics* **2019**, *151* (23), 234101. https://doi.org/10.1063/1.5132354.
(11) Gauthier, J. A.; Ringe, S.; Dickens, C. F.; Garza, A. J.; Bell, A. T.; Head-Gordon, M.; Nørskov, J. K.; Chan, K. Challenges in Modeling Electrochemical Reaction Energetics with Polarizable Continuum Models. *ACS Catalysis* **2019**, *9* (2), 920–931. https://doi.org/10.1021/acscatal.8b02793.
(12) Nørskov, J. K.; Rossmeisl, J.; Logadottir, A.; Lindqvist, L.; Kitchin, J. R.; Bligaard, T.; Jónsson, H. Origin of the Overpotential for Oxygen Reduction at a Fuel-Cell Cathode. *J. Phys. Chem. B* **2004**, *108* (46), 17886–17892. https://doi.org/10.1021/jp047349j.
(13) Gauthier, J. A.; Dickens, C. F.; Heenen, H. H.; Vijay, S.; Ringe, S.; Chan, K. Unified Approach to Implicit and Explicit Solvent Simulations of Electrochemical Reaction Energetics. *J. Chem. Theory Comput.* **2019**, *15* (12), 6895–6906.
(14) Vijay, S.; Ju, W.; Brückner, S.; Tsang, S.-C.; Strasser, P.; Chan, K. Unified Mechanistic Understanding of CO2 Reduction to CO on Transition Metal and Single Atom Catalysts. *Nature Catalysis* **2021**, *4* (12), 1024–1031. https://doi.org/10.1038/s41929-021-00705-y.
(15) Gauthier, J. A.; Dickens, C. F.; Ringe, S.; Chan, K. Practical Considerations for Continuum Models Applied to Surface Electrochemistry. *ChemPhysChem* **2019**, *20* (22), 3074–3080.
(16) Chen, J.; Li, C.; Shi, G. Graphene Materials for Electrochemical Capacitors. *The Journal of Physical Chemistry Letters* **2013**, *4* (8), 1244–1253. https://doi.org/10.1021/jz400160k.
(17) Choi, C. H.; Lim, H.-K.; Chung, M. W.; Chon, G.; Ranjbar Sahraie, N.; Altin, A.; Sougrati, M.-T.; Stievano, L.; Oh, H. S.; Park, E. S.; Luo, F.; Strasser, P.; Dražić, G.; Mayrhofer, K. J. J.; Kim, H.; Jaouen, F. The Achilles' Heel of Iron-Based Catalysts during Oxygen Reduction in an Acidic Medium. *Energy Environ. Sci.* **2018**, *11* (11), 3176–3182. https://doi.org/10.1039/C8EE01855C.
(18) Gu, J.; Hsu, C.-S.; Bai, L.; Chen, H. M.; Hu, X. Atomically Dispersed Fe3+ Sites Catalyze Efficient CO2 Electroreduction to CO. *Science* **2019**, *364* (6445), 1091–1094.
(19) Wang, J.; Huang, Z.; Liu, W.; Chang, C.; Tang, H.; Li, Z.; Chen, W.; Jia, C.; Yao, T.; Wei, S.; others. Design of N-Coordinated Dual-Metal Sites: A Stable and Active Pt-Free Catalyst for Acidic Oxygen Reduction Reaction. *J. Am. Chem. Soc.* **2017**, *139* (48), 17281–17284.
(20) Ren, W.; Tan, X.; Yang, W.; Jia, C.; Xu, S.; Wang, K.; Smith, S. C.; Zhao, C. Isolated Diatomic Ni-Fe Metal–Nitrogen Sites for Synergistic Electroreduction of CO2. *Angew. Chem. Int. Ed.* **2019**, *58* (21), 6972–6976.
(21) Medford, A. J.; Shi, C.; Hoffmann, M. J.; Lausche, A. C.; Fitzgibbon, S. R.; Bligaard, T.; Nørskov, J. K. CatMAP: A Software Package for Descriptor-Based Microkinetic Mapping of Catalytic Trends. *Catalysis Letters* **2015**, *145* (3), 794–807. https://doi.org/10.1007/s10562-015-1495-6.
(22) Bagger, A.; Ju, W.; Varela, A. S.; Strasser, P.; Rossmeisl, J. Electrochemical CO2 Reduction: A Classification Problem. *ChemPhysChem* **2017**, *18* (22), 3266–3273.